


# Towards a higher mass for NGC1052-DF2: an analysis based on full distribution functions

Adi Nusser<sup>1,2</sup> 

<sup>1</sup>*Department of Physics and the Asher Space Research Institute, Israel Institute of Technology Technion, Haifa 32000, Israel*

<sup>2</sup>*Guangdong Technion-Israel Institute of Technology, Shantou 515063, P.R.China*

16 June 2022

## ABSTRACT

It is demonstrated that the kinematics of the 10 star clusters in NGC1052-DF2 is compatible with a high dynamical mass close to those implied by the standard stellar-to-halo-mass-ratio (SHMR). The analysis relies on a convenient form for the distribution function (DF) of projected phase space data, capturing non-gaussian features in the spread of true velocities of the mass tracers. A key ingredient is tidal stripping by the gravity of the apparently nearby larger galaxy, NGC1052. Tidal stripping decreases the range of velocities of mass tracers, while only mildly lowering the total mass inside the trimming radius  $r_{\text{tr}}$ . For the fiducial value  $r_{\text{tr}} = 10$  kpc, we find that the virial mass of the pre-trimmed halo is  $M < 1.5 \times 10^{10} M_{\odot}$  at  $2\sigma$  (95%) and  $M < 8 \times 10^9 M_{\odot}$  at  $1.64\sigma$  (90%). For the mass within 10 kpc we obtain,  $M_{10\text{kpc}} < 3.8 \times 10^9 M_{\odot}$  and  $< 2.5 \times 10^9 M_{\odot}$  at  $2\sigma$  and  $1.64\sigma$ , respectively. The  $2\sigma$  upper limit on the virial mass is roughly a factor of 3-5 below the mean SHMR relation. Taking  $r_{\text{tr}} = 20$  kpc, lowers the  $2\sigma$  mass limits by a factor of  $\sim 4$ .

**Key words:** galaxies: halos - cosmology: theory, dark matter

## 1 INTRODUCTION

Assuming it is at a distance of  $\approx 20$ , the galaxy NGC1052-DF2 exhibits several interesting properties. The galaxy hosts 10 star clusters with luminosities similar to globular clusters found in brighter galaxies (van Dokkum et al. 2018a). Particularly intriguing is the low velocity dispersion derived from the line-of-sight (l.o.s) of the 10 star clusters. Within the framework of Newtonian gravity, all *best-fit* mass models require little dark matter (DM) (van Dokkum et al. 2018a; Martin et al. 2018; Wasserman et al. 2018; Hayashi & Inoue 2018), in great contrast to the mass inferred from the stellar content of the galaxy. Indeed, matching the NGC1052-DF2 stellar content of  $\sim 2 \times 10^8 M_{\odot}$  is an SHMR dynamical mass close to  $10^{11} M_{\odot}$ . This places the galaxy at the extremes of galaxy formation models designed in the framework of the  $\Lambda$ CDM scenario. However, the small number of tracers, missing 3D positions and large l.o.s velocity errors, leave little prospect for a robust measurement of the actual mass of the system. A less ambitious question is whether a high mass close to the SHMR can indeed be ruled out with a high confidence level? In contrast to previous studies we attempt to answer this question using a formalism based on full distribution functions (DFs) of the observed projected phase space of tracers. We also take into account the effect of the removal of outer parts of the galaxy by the action of external gravitational tides. We will assume that the NGC1052-DF2 is originally associated with a high halo mass, which had lost (or never accreted) mass beyond

a radius  $r_{\text{tr}}$ , because of the action of the gravitational tidal field of a nearby larger galaxy. As a fiducial value we consider  $r_{\text{tr}}$  which is consistent with the extent of both the observed surface brightness of NGC1052-DF2 and the distribution of the star clusters. We do not require that the mass inside this radius is decreased and we will assume that it remains the same. We explore the virial mass of the original halo and the mass within  $r_{\text{tr}}$ , using the projected phase space data of projected distances and l.o.s velocities of the 10 star clusters. There are several methods for inferring mass from projected phase space data (e.g. Mamon et al. 2013). Here we employ certain assumptions that will allow us to express the distribution function of projected phase space variables in a simple and compact form. The DF allows a construction of a likelihood function of data, without invoking additional assumptions on moments of the true l.o.s velocities.

The distance to NGC1052-DF2 is required to convert measured angular separations into projected distances of tracers and to derive the stellar mass from the 2D stellar distribution. There is an ongoing debate regarding the distance to NGC1052-DF2. The distance of  $D \approx 20$  Mpc reported by van Dokkum et al. (2018a) has been disputed by Trujillo et al. (2018) who argue in favor of  $D \approx 13$  Mpc. More recently, a new distance of  $D = 18.7 \pm 1.7$  Mpc is provided by van Dokkum et al. (2018c). Deeper observations the color magnitude diagram should yield a complete resolution to the distance conundrum. The nearer distance leads a smaller stellar mass ( $\sim 6 \times 10^7 M_{\odot}$ ) and, thus, brings NGC1052-DF2 closer to the standard SHMR (Trujillo et al. 2018). Therefore, the main interest is in the mass models for  $D = 20$  Mpc and here

\* E-mail: adi@physics.technion.ac.il

we opt to present results for this distance only. We only mention that the actual constraints on the virial halo mass are not significantly different from  $D = 13$  Mpc.

The outline of the remainder of the paper is as follows. The methodology of constructing the DFs of the observables is described in §2. In §3, the mass model of NGC1052-DF2 is presented in terms of a stellar component embedded in a DM halo. This section also includes a detailed description of the effect of tidal stripping. The §4 gives the upper limits obtained from our DF based likelihood function. The paper is concluded with a discussion in §5.

## 2 OBSERVABLES AND DISTRIBUTION FUNCTIONS

We assume that the galaxy is in a steady state where the mass distribution is probed by a sample of tracers with measured l.o.s. velocity,  $u_0$ , and projected (perpendicular to the l.o.s) distances,  $R_0$ , with respect to the galaxy center. The true values of these observables are denoted simply by  $u$  and  $R$ . We assume that the measurement errors in  $R_0$  are negligible. As in Wasserman et al. (2018), we introduce  $u_{\text{sys}}$  to allow for uncertainties in the determination of the systemic velocity. Thus, we write, for tracer  $i$ ,

$$R_{0i} = R_i, \quad (1)$$

and

$$u_{0i} = u_i + u_{\text{sys}} + \delta u_i, \quad (2)$$

where  $\delta u_i$  are the individual measurement errors.

The likelihood function,  $\mathcal{L}(u_0, R_0)$  for observing  $u_0$  and  $R_0$  is then written as

$$\mathcal{L} = \int du_{\text{sys}} P(u_{\text{sys}}) \prod_i \int du_i G(u_{0i} | u_i + u_{\text{sys}}) F(u_i, R_{0i}). \quad (3)$$

We take the probability distribution function  $P(u_{\text{sys}})$  to be a Gaussian with the mean of the observed velocities and a standard deviation of  $5 \text{ km s}^{-1}$  (Wasserman et al. 2018). Also  $G$  is a Gaussian with mean  $u_i + u_{\text{sys}}$  and *rms* scatter  $\sigma_{ui}$  representing the random error  $\delta u_i$  in measuring  $u_{0i}$ . The main challenge in computing  $\mathcal{L}$  is the distribution function (hereafter DF),  $F$ , of the underlying quantities  $u$  and  $R$ . We describe below our derivation of  $F$  from a given mass model for the galaxy. Constraints on the mass model will then be obtained by maximizing  $\mathcal{L}$  with respect to the parameters of this model.

The unknown velocity in the projected plane is denoted by  $\mathbf{w}$  with an amplitude  $w$ . Thus the 3D velocity of a tracer is  $\mathbf{v} \equiv \mathbf{w} + u\hat{\mathbf{z}}$ , where the l.o.s is arbitrarily chosen as the positive  $z$  axis. Assuming azimuthal symmetry,  $F(u, R)$  will be derived from a model for the DF,  $f(\mathbf{v}, \mathbf{r})$ , of the full phase space information of 3D velocities and positions. This is done, first by computing the DF,  $f_u(u, \mathbf{r})$ , of the line-of-sight velocity component and the 3D distance  $r$ ,

$$f_u(u, \mathbf{r}) = \int d^2\mathbf{w} f(\mathbf{v}, \mathbf{r}). \quad (4)$$

Then  $F$  is obtained using

$$F(u, R) = \int dz f_u(u, R, z). \quad (5)$$

### 2.1 The ergodic DF

We adopt the definitions

$$\mathcal{E} = \Psi - v^2/2 \quad \text{and} \quad \Psi = -\Phi, \quad (6)$$

where  $v^2 = u^2 + w^2$  and  $\Phi$  is the gravitational potential generated by all components of the system. We assume now that the full phase space DF is of the form  $f(\mathbf{v}, \mathbf{r}) = f(\mathcal{E})$ . This form of the steady state DF implies spherical symmetry as well as isotropic velocity distribution and is appropriately termed “ergodic” by Binney & Tremaine (2008). We further impose  $\Psi \rightarrow 0$  as  $r \rightarrow \infty$  and  $f(\mathcal{E}) = 0$  for  $\mathcal{E} \leq 0$ . Then, the function  $f(\mathcal{E})$  obeys (e.g. Binney & Tremaine 2008),

$$f(\mathcal{E}) = \frac{1}{\sqrt{8\pi^2}} \frac{d}{d\mathcal{E}} \int_0^{\mathcal{E}} \frac{d\Psi}{\sqrt{\mathcal{E}-\Psi}} \frac{d\nu}{d\Psi}, \quad (7)$$

where  $\nu(r)$  is the distribution of mass tracers and  $d\nu/d\Psi = (d\nu/dr)(d\Psi/dr)^{-1}$ .

The DF,  $f_u$  is obtained from Eq. 4, by integrating  $f$  over the projected velocity where  $d^2\mathbf{w} = 2\pi w dw$ ,

$$f_u(u, r) = 2\pi \int w dw f(\mathcal{E}). \quad (8)$$

At fixed  $r$  and  $u$  we have  $d\mathcal{E} = w dw$  and thus,

$$f_u(u, r) = 2\pi \int_0^{\mathcal{E}_m} d\mathcal{E} f(\mathcal{E}), \quad (9)$$

where

$$\mathcal{E}_m = \Psi(r) - \frac{u^2}{2} \quad (10)$$

corresponds to  $w = 0$ . Together with Eq. 7 we then arrive at

$$f_u(u, r) = \frac{1}{\sqrt{2\pi}} \int_0^{\mathcal{E}_m} \frac{d\Psi}{\sqrt{\mathcal{E}_m - \Psi}} \frac{d\nu}{d\Psi}, \quad (11)$$

offering a convenient form for deriving  $f_u$  from  $\Psi$  and  $\nu$  under the assumption of ergodicity.

### 2.2 DF for circular orbits

An ergodic DF corresponds to an isotropic velocity dispersion. In complete contrast, is the case of particles moving on circular orbits where the velocity of a tracer is perpendicular to  $\mathbf{r}$ , with a magnitude  $V_c(r) = GM(< r)/r$ . Let  $\theta$  be the angle between  $\mathbf{r}$  and the  $z$  axis and  $\phi$  be the azimuthal angle between the  $x$  axis and the projection of  $\mathbf{r}$  onto the  $xy$  plane. Taking  $\eta$  to be the angle between  $\mathbf{v}$  and the azimuthal direction, we find

$$u = V_c(r) \sin \theta \sin \eta \quad (12)$$

We write the DF of  $u$  and  $\mathbf{r}$  as  $f_u^{\text{circ}}(u, \mathbf{r}) = P(u|\mathbf{r})\nu(r)$  where the probability distribution function (PDF)  $P(u|\mathbf{r})$  can be expressed in terms of the PDF,  $P_\eta$ , for  $\eta$  as

$$P(u|\mathbf{r}) = P_\eta \frac{d\eta}{du}. \quad (13)$$

Clearly  $P(u|\mathbf{r}) = 0$  for  $|u| > V_c \sin \theta$ . Otherwise,

$$P(u|\mathbf{r}) = \frac{P_\eta}{\sqrt{V_c^2 \sin^2 \theta - u^2}} \quad (14)$$

where we have used  $\cos \eta = \sqrt{1 - u^2/V_c^2 \sin^2 \theta}$ . A uniform  $P_\eta = \text{const}$ , yields isotropic velocity dispersion in the tangential direction, i.e.  $\sigma_\phi^2 = \sigma_\theta^2$  and corresponds to

$$P(u|\mathbf{r}) = \frac{1}{\pi} \frac{1}{\sqrt{V_c^2 \sin^2 \theta - u^2}}, \quad (15)$$

which has a minimum of  $P(u|\mathbf{r})$  at  $u = 0$  and diverges as  $|u| \rightarrow V_c \sin \theta$ . Alternatively, the choice  $P_\eta \propto |\cos \eta|$  leads to  $\sigma_\phi^2 = 2\sigma_\theta^2$  and

$$P(u|\mathbf{r}) = \frac{1}{2V_c \sin \theta}, \quad (16)$$

which is uniform for  $|u| \leq V_c \sin \theta$  and zero otherwise. For  $P_\eta \propto \cos^2 \eta$  we obtain  $\sigma_\phi^2 = 3\sigma_\theta^2$  and

$$P(u|\mathbf{r}) = \frac{2}{\pi} \frac{\sqrt{1 - u^2/V_c^2 \sin^2 \theta}}{V_c \sin \theta}. \quad (17)$$

Using  $\sin \theta = R/\sqrt{R^2 + z^2}$  we write the DF,  $f_u^{\text{circ}} = \nu P(u|\mathbf{r})$  as

$$f_u^{\text{circ}}(u|\mathbf{r}) = \nu(r)P(u|R, z). \quad (18)$$

Integrating this function along the l.o.s. as in Eq. 5 gives the corresponding  $F(u, R)$ . Note that although  $\nu$  is assumed to be spherically symmetric, the last expression remains valid also for azimuthal symmetry, i.e.  $\nu = \nu(R, z)$ .

### 3 MASS MODEL

We model the galaxy as a two component system of stars and DM, both assumed spherical. The DM component is assumed to follow the Navarro-Frenk-White (NFW) density profile (Navarro et al. 1996), with parameters consistent with the structure of halos identified in cosmological simulations (e.g. Gao et al. 2008; Ludlow et al. 2013; Dutton & Maccio 2014; Diemer & Kravtsov 2015). We define  $r_{200}$  as the radius of the sphere within which the mean halo density is 200 times the critical density  $\rho_c = 3H^2/8\pi G$ . We treat  $r_{200}$  as the virial radius and the mass  $M = M_{200}$  inside  $r_{200}$  as the virial mass (ignoring small differences with other definitions of the virial mass). In addition to the mass, the second and only other parameter needed to specify the NFW profile is the concentration parameter,  $C$ . We adopt the fitting formula for the concentration-mass relation,  $\bar{C}(M)$ , found by Dutton & Maccio (2014) for halos identified in simulations. As shown by Wasserman et al. (2018), the observed kinematics of NGC1052-DF2 favors small concentrations for models with large halo masses. Since we seek the highest virial halo mass consistent with the NGC1052-DF2 kinematics, we will consider the lowest concentration which remains compatible with the scatter around the mean  $\bar{C}(M)$ , as found in simulations. A concentration of 40% below  $\bar{C}(M)$ , falls roughly within a  $1\sigma$  scatter (e.g. Gao et al. 2008; Ludlow et al. 2013). Thus, we will provide results for  $C = \bar{C}(M)$  and also for lower values  $C = 0.6\bar{C}$ . We could also work with the Einasto profile which is a more general fit to the halo structure. However, this profile involves a third parameter, the power index  $\alpha_E$ . Although, for the relevant mass range,  $\alpha_E$  has a very weak dependence on mass, converging to  $\alpha_E = 0.167$ , the scatter is important and we lack a quantification of the covariance between the concentration and the power index (e.g. Dutton & Maccio 2014). Therefore, for our purposes here we prefer to work with the 2 parameter NFW fit to describe the DM halo.

As for the stellar component, we adopt an Einasto profile with parameters  $r_{200} = 10$  kpc,  $C_E = 8.1$  and  $\alpha_E = 0.4$ . As shown in (Nusser 2018), this profile yields an excellent fit to the observed two-dimensional (2D) structure of NGC1052-DF2 represented as a Sérsic profile with index  $n_S = 0.6$  and half-light radius  $R_e \approx 2.2$  kpc. The stellar mass is normalized to  $2 \times 10^8 M_\odot$ , in accordance with the observations.

It is instructive to examine the difference between the low and

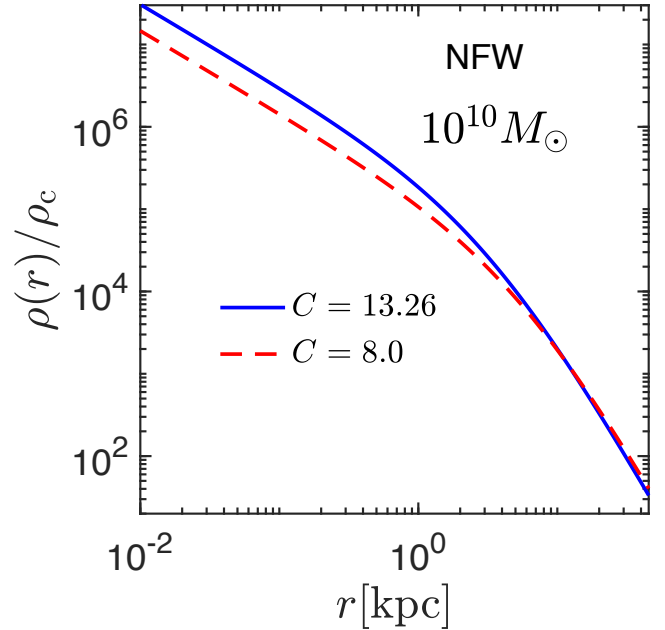


**Figure 1.** NFW mass profiles for two values of the concentration parameter. The high concentration corresponds to the mean value obtained in N-body simulations, while the other value is 40% lower.

high concentration NFW profiles considered here. Fig. 1 plots profiles for a halo with  $M_{200} = 10^{10} M_\odot$ , for  $C = \bar{C} \approx 13.26$  and a 40% lower value,  $C \approx 8$ . The virial radius is  $r_{200} = 46$  kpc, but the profiles are close to each other down to  $r \sim 5$  kpc, which is roughly the radius of the inner region probed by the observed kinematics of the 10 star cluster in NGC1052-DF2.

#### 3.1 Tidal stripping/trimming: reduction of velocity dispersion

Crucial to the mass modeling is the assumption that NGC1052-DF2 had been stripped of matter outside a radius of  $\sim 10$  kpc, by the tides of external gravitational forces. As we will see below, the net effect of that is a reduction in the velocity dispersion, while maintaining almost the same amount of interior mass. At  $D \approx 20$  Mpc, NGC1052-DF2 is likely associated with the much larger galaxy NGC1052. This large elliptical galaxy is a reasonable candidate for supplying the necessary gravitational tides. It should be pointed out that the relative radial velocity of NGC1052-DF2 relative to NGC1052 is  $293 \text{ km s}^{-1}$  (van Dokkum et al. 2018a), while the l.o.s velocity dispersion of the NGC1052 group is only  $110 \text{ km s}^{-1}$  (van Dokkum et al. 2018a) which is consistent with the circular velocity of  $V_c = 200 \text{ km s}^{-1}$  measured from the H I content of NGC1052 Gorkom1986. Thus the relative speed of NGC1052-DF2 is close to the escape velocity from NGC1052. At a projected distance of 100 kpc between the two galaxies, NGC1052-DF2 is likely to be just skimming past NGC1052. However, a larger mass for NGC1052 is obtained from the SHMR relation. For NGC1051 stellar mass of  $\sim 10^{11} M_\odot$ , the SHMR gives a dynamical mass of  $\sim 5 \times 10^{12} M_\odot$  (Wasserman et al. 2018), corresponding to  $V_c \sim 250 \text{ km s}^{-1}$ . In any case, there is a large uncertainty in the estimation of the tidal radius of NGC1052-DF2 in the presence of NGC1052 (Ogiya 2018; Wasserman et al. 2018).

Nevertheless, a tidal radius of  $\sim 10$  kpc is consistent with the observed spatial extent of the stellar component of NGC1052-DF2 and the distribution of the projected distances of its star clusters.

Particles with high apocenters reaching the inner regions move faster than those bound to inner orbits. Thus, excising the outer particles, narrows the range of velocities in the inner regions. To illustrate this point, without offering a realistic quantification of the effect, we resort to a simulation of an isolated halo of mass  $M_{200} = 1.3 \times 10^{10} M_{\odot}$ . The simulation is similar to those used by Nusser (2018) to study the effect of dynamical friction of the population of the star clusters in NGC1052-DF2. The simulation contains  $2.4 \times 10^5$  particles of equal mass, distributed according to the Einasto mass profile. The particles were advanced forward for 10 Gyr using the publicly available *treecode* by (Barnes & Hut 1986). Further details can be found in Nusser (2018). We select those particles found at distances of less than a trimming radius  $r_{\text{tr}} = 10$  kpc from the halo center in all 50 snapshots covering the last 5 Gyr of the simulation. We assume that those particles were never at a farther distance and we identify them as composing the halo surviving a tidal stripping process. We then project the particle velocities along a single axis (the l.o.s) and compute the corresponding velocity dispersion,  $\sigma_u$ , at a 3D distance  $r$  from the center. We compare this with the velocity dispersion computed from all original particles (i.e. including pre-trimming particles passing by from distances beyond 10 kpc). The red and blue solid curves in the top panel of Fig. 2 plot velocity dispersions versus  $r$  for the trimmed (tidally stripped) and the untrimmed halos. The l.o.s velocity variance  $\sigma_u^2$  is represented by the solid curves. As  $r$  approaches the trimming radius of 10 kpc,  $\sigma_u^2$  of the trimmed halo (red solid curve) falls substantially below the untrimmed halo (blue solid). The ratio of  $\sigma_u^2$  between the two curves approaches unity only at  $r < 2$  kpc. The dotted curves represent the variance,  $\sigma_r^2$ , of the radial (from the halo center) velocity component. The red dotted curve actually drops to zero at 10 kpc, since there are no particles moving beyond that radius. The dashed curves are the tangential velocity variance divided by 2,  $\sigma_t^2 = (\sigma_{\theta}^2 + \sigma_{\phi}^2)/2$ . Trimming also reduces the tangential dispersion but the reduction in the  $\sigma_u^2$  is mainly due to the lowered dispersion in the radial direction. Note that the velocity dispersion ellipsoid in the original halo is skewed to the tangential direction, with an anisotropy parameter  $\beta = 1 - \sigma_t^2/2\sigma_r^2 \approx -0.7$  for  $2 \lesssim r \lesssim 10$  kpc. The reduction in  $\sigma_u$  clearly depends on the parameter  $\beta$  of the original halo. We emphasize that the numerical experiment presented here is simply for illustration purposes. In fact, halos in simulations with generic initial conditions based on the  $\Lambda$ CDM model, have a marked tendency towards a positive  $\beta$  (e.g. Sparre & H. Hansen 2012). This implies both a more significant reduction in  $\sigma_u$  and also a more isotropic velocity ellipsoid in the trimmed halo at  $r < r_{\text{tr}}$ .

The trimming procedure has a much lesser effect on the mass,  $M(r)$ , encompassed within a radius  $r < r_{\text{tr}}$ . The bottom panel of Fig. 2, plots the reduction in the relative mass between the trimmed and the pre-trimmed halos. The reduction is meager and does not exceed 22%, even at  $r = 10$  kpc. Thus, in our modeling of  $F_u$  we will ignore this mild reduction in the mass inside  $r_{\text{tr}}$  and treat the gravitational force field according to the original NFW mass profiles. The effect of tidal stripping will simply be included by imposing a vanishing density outside  $r_{\text{tr}}$ . Tidal stripping is a cumulative process which can be modeled accurately for a known host mass profile and the orbit of the satellite galaxy. Unfortunately, none of these are accessible to us from current observations and therefore, in our “semi-analytic” approach here, we simply trim the halo at a certain radius. Since our modeling is simplified we do not term this

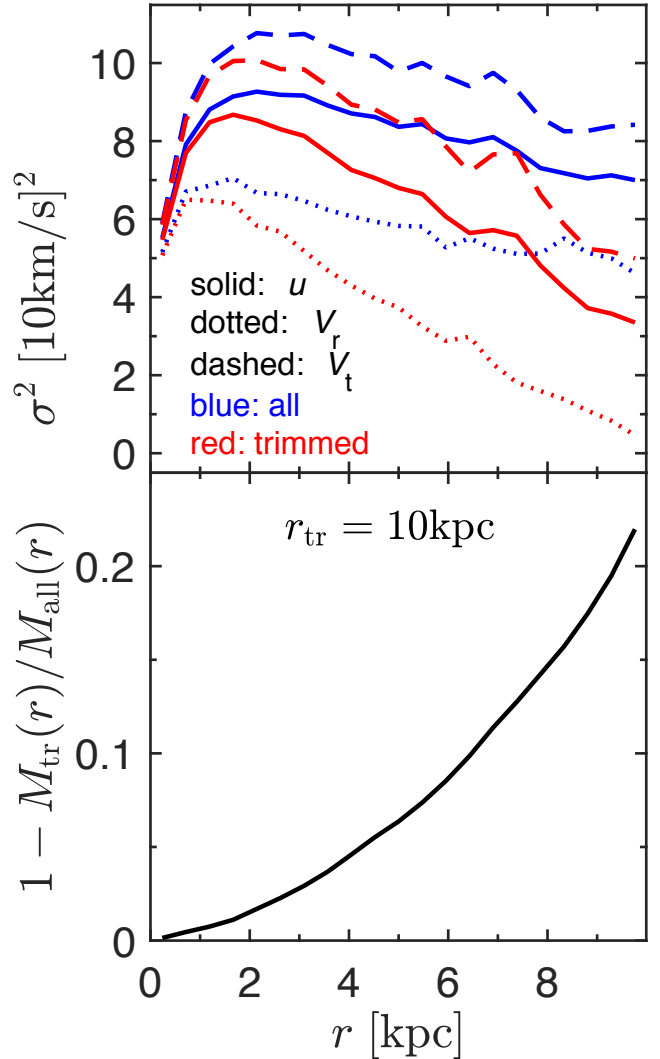


**Figure 2.** *Top:* The variance of velocity, versus the 3D radius, of particles inside a radius of  $r_{\text{tr}} = 10$  kpc in a simulated halo of  $M_{200} = 1.3 \times 10^{10} M_{\odot}$ . The blue curve is the variance from particles in the pre-trimmed halo, where the red curve is only for particles with apocenters smaller than  $r_{\text{tr}}$ . Solid, dotted and dashed curves correspond to velocities in l.o.s, radial and tangential directions, respectively. The variance of the tangential velocity is divided by 2. *Bottom:* Relative reduction of mass within  $r$  due to removal of particles outside 10 kpc.

radius the tidal radius as is common but rather the trimming radius. In any case, gravitational tidal stripping always results in a radius beyond which the density effectively drops to zero. Fig. 3 gives the useful information of the fraction of the mass,  $M_{10 \text{ kpc}}$  within 10 kpc relative to the virial halo mass.

### 3.2 Distribution of tracers

In addition to the mass model, the calculation of the likelihood function,  $\mathcal{L}$ , in Eq. 3 involves an assumed form for the distribution of tracers,  $\nu(r)$ . In ? and Trujillo et al. (2018), the distribution of the 10 tracer star clusters in NGC1052-DF2 is represented as a power law where the cumulative distribution up-to a distance  $r$  is  $n(r) \propto r^{3-\gamma}$  corresponding to  $\nu \propto r^{-\gamma}$ . We follow these authors and adopt this form.



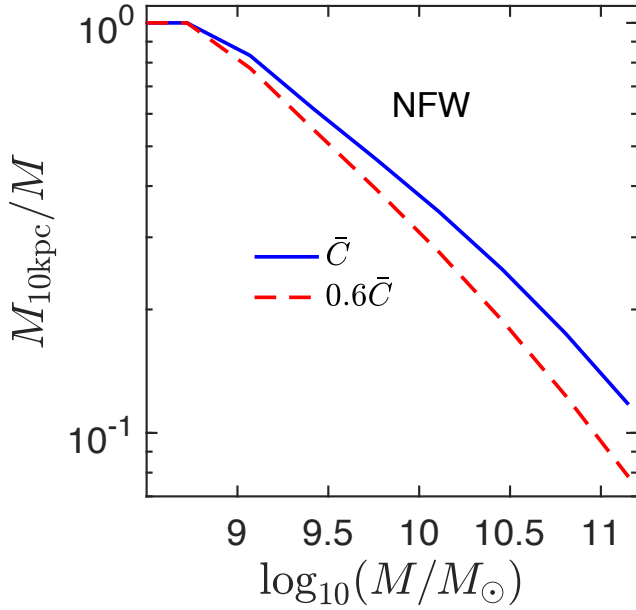


**Figure 3.** The ratio of the mass,  $M_{10\text{kpc}}$ , contained inside a 10 kpc (3D) distance, to the mass  $M = M_{200}$  of the halo. The solid and dashed curves correspond to  $C = \bar{C}(M)$  and  $0.6\bar{C}(M)$ , respectively. For  $r_{200} < 10$  kpc, the ratio is set to unity.

## 4 RESULTS

This section begins with a general illustration of the shape of predicted DFs. Then it describes the way we ascertain the validity of our analysis framework and how confidence levels (CLs) on the relevant parameter are derived. Then, we present the actual implications of the data on the halo mass.

### 4.1 Predictions for the DF

The mass model dictates  $F_u(u, R)$  which, in turn determines the likelihood  $\mathcal{L}$  through Eq. 3. It is thus instructive to examine the behavior of  $F_u(u, R)$  in some detail. Fig. 4 shows curves of  $F_u$  in terms of  $\tilde{u} = \sqrt{3}u/V_c$ , where  $V_c = GM_{200}/r_{200}$ . The calculations are done for halo with  $M_{200} = 1.3 \times 10^{10}$  ( $V_c = 34 \text{ km s}^{-1}$ ),  $C = 0.6\bar{C} = 7.7$  and a power law index of the spatial distribution of tracers with  $\gamma = 2.4$ . The trimming radius is  $r_{\text{tr}} = 10$  kpc, encompassing  $\sim 4 \times 10^9 M_\odot$  in DM (c.f. Fig. 3), in addition to the stellar content. The set of equations in §2.1 is then used to calculate the DF under the ergodic assumption. The DF for circular orbits with isotropic angular distribution is obtained using Eq. 15. We also consider a non-isotropic angular distribution of orbits corresponding to  $\sigma_\phi^2 = 2\sigma_\theta^2$  and Eq. 16. In all these three cases, Eq. 5 is employed to obtain the DF in terms of the projected distance  $R$  rather than the 3D distance  $r$ . The figure shows the PDF  $P(\tilde{u})$  obtained from the DFs at a projected distance  $R = 2.4$  kpc and 7 kpc, as indicated. The PDFs are symmetric with respect to the sign of  $u$  and hence the figure refers only to positive velocities. The ergodic DF, shown as the black solid curve, declines with increasing velocities and matches a Gaussian for  $R = 2.4$  kpc. However, closer to  $r_{\text{tr}}$ , at  $R = 7$  kpc, there is a clear deviation from a Gaussian. At this distance, there is a cutoff at  $u \approx V_c$ , indicating the escape speed. The circular orbit PDF with isotropic distribution (dotted blue) has a distinctive dip at  $u \sim 0$ , diverges around the circular velocity of the halo,  $V_c$ , and vanishes at larger velocities.

The PDF for anisotropic circular orbits (red dashed) is constant at low velocities, in accordance with Eq. 16. However, because of the integration over the l.o.s (see Eq. 5), the PDF declines at large velocities. We already can see that the mass constraints will be lowest for the assumption the isotropic circular orbits. For circular orbits, the trimming radius affects  $F_u$  only through the integration over  $z$  in Eq. 5.

Fig. 5, plots the measured NGC1052-DF2 l.o.s. velocities and the predicted velocity dispersion,  $\sigma_u^2$ , from the ergodic DF for an NFW mass profile with 3 different masses, as indicated in the figure. The prediction depends on  $\gamma$  and hence we plot results for two values of  $\gamma$  for the most massive halo considered in the figure. As expected, the large trimming radius,  $r_{\text{tr}} = 20$  kpc, (right panel) is associated with a higher  $\sigma_u^2$  than  $r_{\text{tr}} = 10$  kpc (left panel). Comparison between the two panels, reveals that trimming has a substantially more pronounced effect on the more massive halos. For the halo with  $M_{200} = 6.3 \times 10^{10} M_\odot$ , the dispersion at  $R = 6$  kpc drops from  $30 \text{ km s}^{-1}$  (left panel) to  $22 \text{ km s}^{-1}$  (right) for  $\gamma = 2.4$  (see dashed curves). For smaller halos, the trimming radius is closer to the virial radius resulting in a much smaller effect. The reduction in  $\sigma_u$  is almost unnoticeable for  $M = 10^9 M_\odot$  (red dash-dotted), where, according to Fig. 3,  $M_{10\text{kpc}}$  is as high as 80% as the original mass,  $M$ . The dependence on  $\gamma$  is actually significant, as seen by comparing the dashed and dotted curves in each panel.

### 4.2 Confidence levels and the goodness of fit

The CLs on model parameters will be set according to the likelihood ratio in terms of  $\Delta\chi^2 = -2\ln \mathcal{L}/\mathcal{L}_{\text{min}}$ , where  $\mathcal{L}_{\text{min}}$  is the minimum over the parameters considered.

Before presenting the results for the CLs, we would like to confirm that parameters corresponding to  $\mathcal{L}_{\text{min}}$  are indeed a good fit to the data- otherwise the whole analysis framework is questionable. An indication for the validity of our analysis can already be seen in Fig. 5 where the dot-dashed curve appear to agree well the velocity measurement. In the following we aim at a more robust validation of our framework.

As it will be seen below (see Fig. 8) that a minimum of  $\mathcal{L}$  is obtained at  $\gamma_{\text{min}} \approx 2.3$  and  $M_{\text{min}} \approx 5 \times 10^8 M_\odot$  for an NFW mass model with  $C = 10.7$  which is 40% lower than the mean concentration for that mass. Using these values, we generate such mocks by drawing random  $u$  from the DF  $F(u, R)$ . Random velocity errors are then added to  $u$  to obtain  $u_0$ . This way we produced a large number of mock catalogs each containing the same number of tracers as the observations. The mock catalogs are then treated as the real data, yielding a  $\mathcal{L}$  value for each mock. As a measure of the goodness-of-fit we examine the agreement of the observed  $\mathcal{L}_{\text{min}}$  with the distribution of  $\mathcal{L}$  from the mocks. Fig. 6 gives the cumulative distribution of  $\tilde{\chi}^2 = -2\ln \mathcal{L}$  from  $10^3$  mocks corresponding to the ergodic DF. The vertical line in the figure, indicating  $\mathcal{L}_{\text{min}}$  from the observations, is clearly consistent with the distribution from mocks, with a  $\lesssim 1\sigma$  from the mean. The result strongly validates our basic modeling framework.

### 4.3 The likelihood $\mathcal{L}$ as a function of $M$ and $C$

Assuming the ergodic DF, we calculate  $\Delta\tilde{\chi}^2$  as a function of the concentration and mass, with fixed  $\gamma = 2.4$  and  $r_{\text{tr}} = 10$  kpc. The results are shown in Fig. 7 by means of contour maps. Only contours of  $\Delta\tilde{\chi}^2 = 1, 2.3, 4, 6.17$  and 9 are plotted. For two degrees of freedom, as our case is, these contours correspond, respectively,

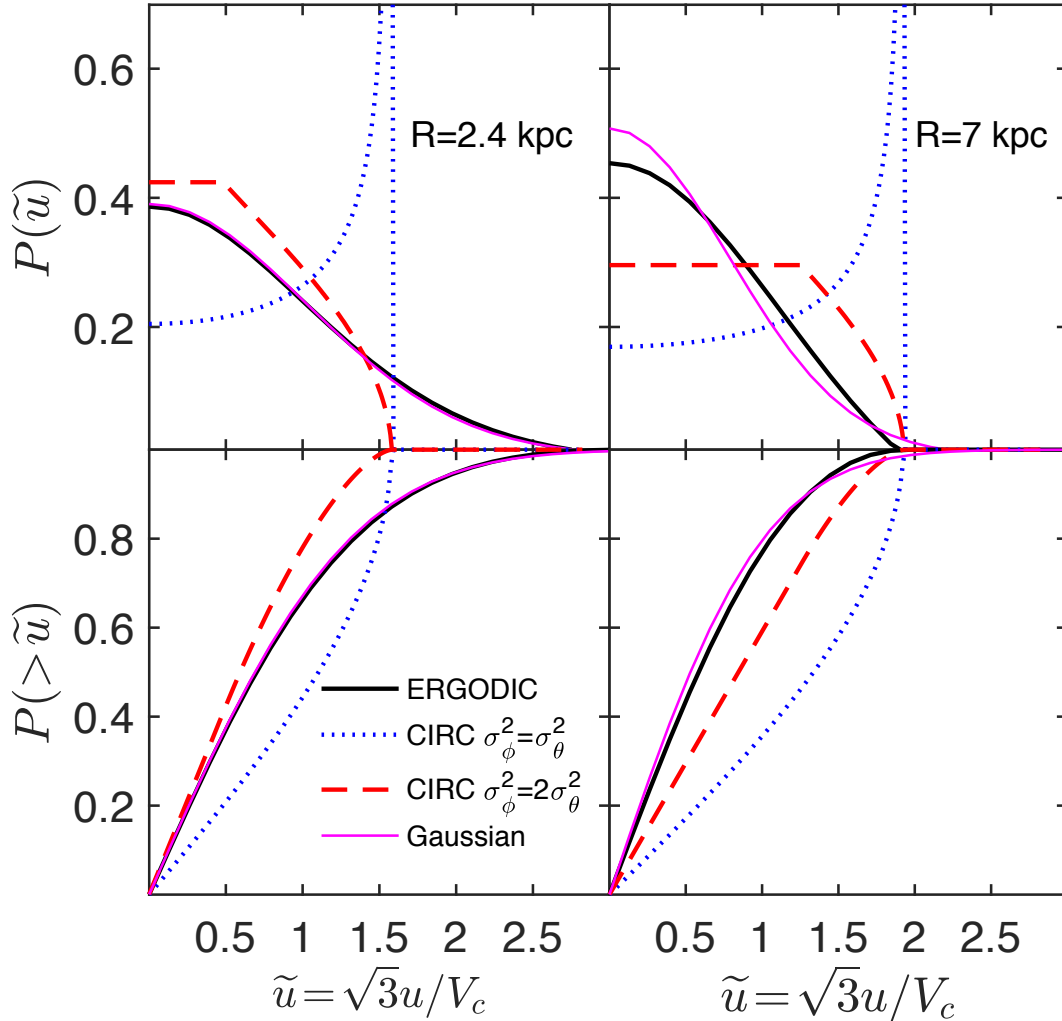


**Figure 4.** The PDF of the l.o.s velocity  $u$  in units of  $V_c/\sqrt{3}$  for tracers at projected distances  $R = 2.4$  kpc (left) and  $7$  kpc (right). Three models are plotted: ergodic (black solid), circular orbits with isotropic angular distribution (dotted blue) and a non-isotropic distribution (dashed red). For comparison, a Gaussian PDF is also shown (solid magenta). The figure corresponds to a DM halo with  $M_{200} = 1.3 \times 10^{10}$  and  $\gamma = 2.4$ . See text.

to CLs of 39%, 68% ( $1\sigma$  for 1D normal distribution), 86% ( $1.52\sigma$ ) 95% ( $2\sigma$ ) and 98.9% ( $2.54\sigma$ ). The data probes a limited region,  $R \lesssim 8$  kpc, associated with a small fraction of the halo mass (see Fig. 3). Unsurprisingly, this leads to a degeneracy between the  $C$  and either  $M_{10\text{kpc}}$  or the virial mass. The degeneracy is naturally more pronounced for  $M_{10\text{kpc}}$ , as implied by the steeper vertical orientation of the blue dotted contours.

The degeneracy can be broken by multiplying  $\mathcal{L}$  by a prior PDF of  $C$  (Wasserman et al. 2018), taken from the concentrations measured from halos in simulations. However, constraints on  $C$  obtained this way, are entirely driven by the prior. For the remainder of the paper, we proceed in a different path, as described next.

#### 4.4 $\mathcal{L}$ as a function of $M$ and $\gamma$

We are primarily motivated by the question of whether the kinematics of NGC1052-DF2 rules out a parent halo with a mass close to the SHMR. According to Fig. 7, smaller masses are associated with high concentrations. Therefore, to assess the compatibility a mass

$M$  with the NGC1052-DF2 observations as well as the SHMR, it is sufficient to consider only an acceptable low  $C$  value. As suggested in §3, we set the low value to  $C = 0.6\bar{C}(M)$  which falls below the mean relation,  $C = \bar{C}(M)$  at the  $\sim 1\sigma$ , as seen for simulated halos. For comparison, we will also consider  $C = \bar{C}(M)$ . The power index,  $\gamma$ , of the assumed power law distribution of tracers affects the DF and thus we treat it as a second parameter, in addition to the mass. We proceed with  $\mathcal{L}$  computed for an array of  $M$  and  $\gamma$ . The lowest  $M$  we consider is  $10^8 M_\odot$ , close to the stellar mass of NGC1052-DF2.

Contours of CLs in the  $\gamma - M$  plane are plotted in Fig. 8. The figure refers to the ergodic DF, where the top panel is for the fiducial  $r_{\text{tr}} = 10$  kpc and the bottom is for  $r_{\text{tr}} = 20$  kpc. Solid and dotted contours in each panel represent NFW mass models with  $C = 0.6\bar{C}(M)$  and  $\bar{C}(M)$ , as indicated in the figure. As in Fig. 7, CL contours for 5 values of  $\Delta\tilde{\chi}^2$  are drawn. As expected, the higher concentration value (dotted curves) produces contours which are more squeezed to lower masses. Note that the  $\Delta\tilde{\chi}^2 = 6.17$  solid contour ( $C = 0.6\bar{C}(M)$ ) roughly overlaps with  $\Delta\tilde{\chi}^2 = 9$  dotted

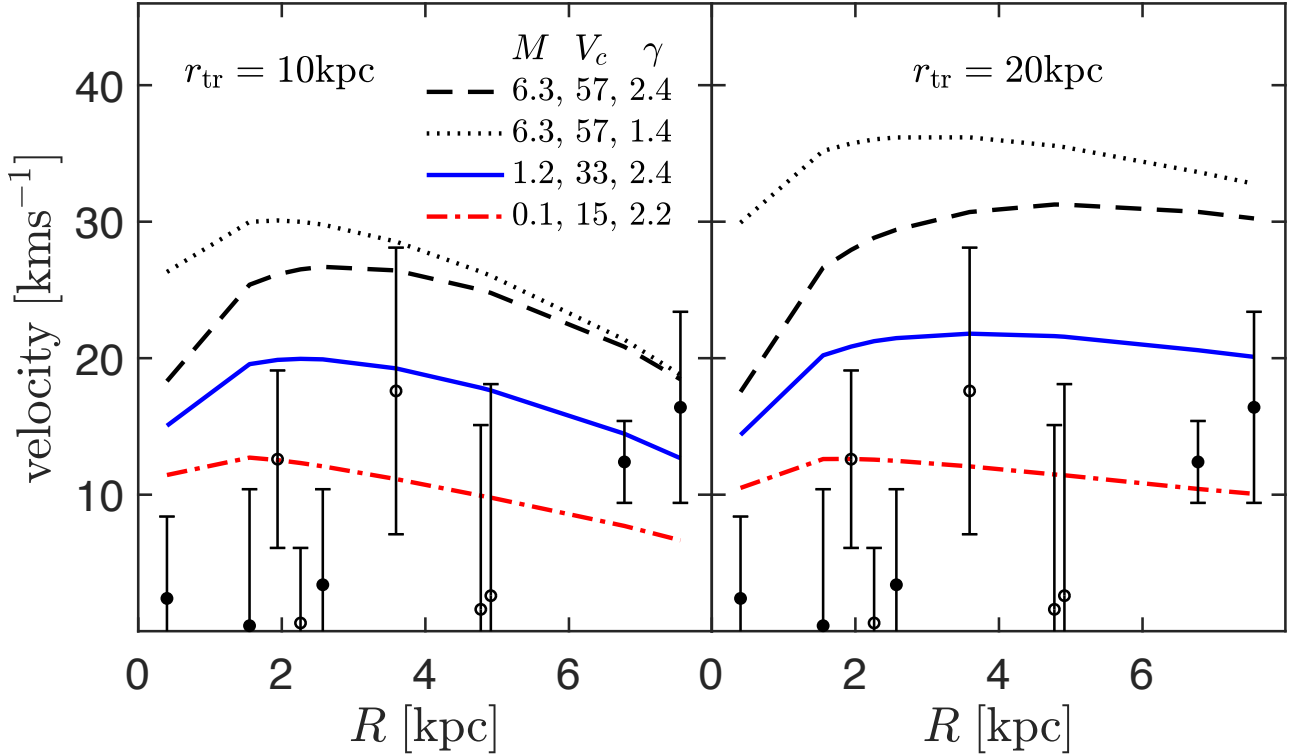


**Figure 5.** The predicted l.o.s velocity dispersion from the ergodic DF, versus projected distance, an NFW profile with  $C = 0.6\bar{C}(M)$ . The *left* panel for a trimming radius  $r_{\text{trim}} = 10$  kpc, while  $r_{\text{trim}} = 20$  kpc is plotted in the *right* panel. Presented are results for 3 choices of the halo mass  $M = M_{200}$ , as indicated in the figure in units of  $10^{10} M_{\odot}$ . The corresponding halo circular velocity  $V_c$  is in  $\text{km s}^{-1}$ . For the highest mass, we plot curves representing two values of  $\gamma$ , as indicated. Points with error-bars are the observed velocities and  $1\sigma$  error-bars from (Wasserman et al. 2018), where filled and open circles correspond, respectively, to positive and negative velocities relative to the mean. The error bars do not include uncertainties due to the systemic velocity.

curve ( $C = \bar{C}(M)$ ). The bending up of the contours with increasing  $M$ , indicates that the constraints on  $\gamma$  are not merely from the observed distribution of projected distances, but also through the kinematical effect of  $\gamma$  on the DF. Still, the dependence on  $M$  is weak and the distribution of the projected distances is nonetheless the main probe of  $\gamma$ . At  $M = 10^9 M_{\odot}$  we find  $\gamma \approx 2.33 \pm 0.35$ , consistent with the result of Trujillo et al. (2018). The trimming radius plays a pivotal role, with the larger  $r_{\text{tr}}$  yielding a factor of  $\sim 4$  lower masses for  $\Delta\chi^2 = 4$ . The break in the shape of the contours in the lower panel at  $\log_{10} \approx 9$  reflects the fact that trimming does not affect small halos with  $r_{200} < 20$  kpc. We also have calculated  $\mathcal{L}$  assuming circular orbits. The results are shown in Fig. 9 where, in both panels, the fiducial  $r_{\text{tr}} = 10$  kpc is used in computing the CLs. In a spherical system, the 3D velocity of a particle on a circular orbit is determined by the enclosed mass. Thus the dependence of DF of the observables and hence also the likelihood on the trimming radius, is weaker and arises only from the geometrical projection effects. The bottom panel corresponds to orbits with random orientations and hence, an isotropic tangential velocity dispersions, with  $\sigma_{\phi}^2 = \sigma_{\theta}^2$  where, as in §2.2,  $\theta$  and  $\phi$  are defined assuming the l.o.s is in the  $z$  direction. In the top panel, a mild anisotropy, in the orientation of the orbits with respect to the l.o.s., is invoked (cf. §2.2 for details). The anisotropy leads to  $\sigma_{\phi}^2 = 2\sigma_{\theta}^2$ , and subsequently a lowering of  $\sigma_u^2$ , in accordance with the curves of the DFs in Fig. 4.

#### 4.5 Upper limits on the mass

For the purpose of deriving upper limits on the mass, we consider  $\Delta\chi^2(\gamma_M, M)$ , where  $\gamma_M$  is the “best-fit” value of  $\gamma$  rendering a maximum  $\mathcal{L}(\gamma, M)$  for a given  $M$ . Thus we treat  $\gamma$  as a “nuisance” parameter using the *profile-likelihood* approach<sup>1</sup>.

We seek upper limits on the DM halo mass for our adopted NFW profile with  $C = 0.6\bar{C}(M)$ . The solid curve in Fig. 10 plots  $\Delta\chi^2(\gamma_M, M)$  for this profile. The dashed and dotted curves correspond, respectively, to results obtained with  $r_{\text{tr}} = 20$  kpc and  $r_{\text{tr}} = 10$  kpc with a high concentration. Mass upper limits from these curves are given in the Table.

For  $r_{\text{tr}} = 10$  kpc, similar  $M_{10\text{kpc}}$  are obtained for both choices of the concentration, although there is a factor of 2 difference in the inferred  $M_{200}$ . This is a reflection of the absence of mass tracers beyond  $R \sim 10$  kpc and, therefore, the more observationally constrained quantity is  $M_{10\text{kpc}}$ . As we have seen in the contour maps, the results are highly sensitive to  $r_{\text{tr}}$ . Maintaining the low concentration, the  $1\sigma$  upper limit on the mass is lowered by a factor  $\sim 20$  for  $r_{\text{tr}} = 20$  kpc relative to  $r_{\text{tr}} = 10$  kpc.

<sup>1</sup> This approach is equivalent to *marginalization* for normal forms of  $\mathcal{L}$  and of the assume prior PDF of  $\gamma$ .

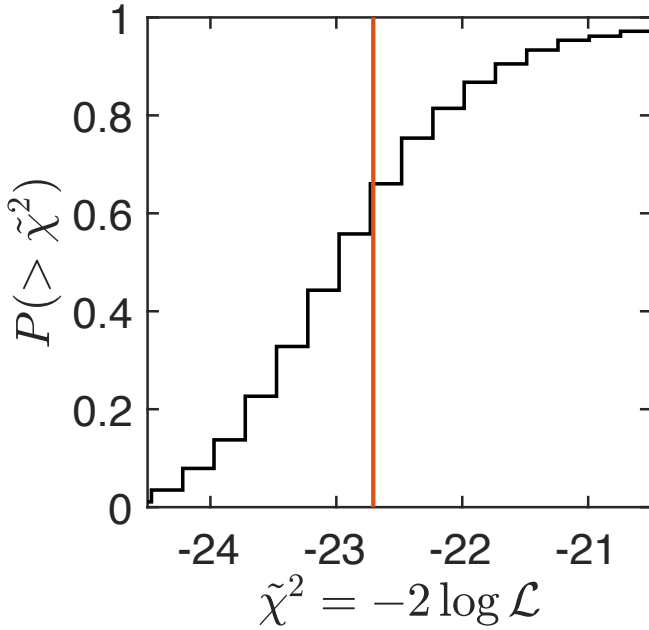


**Figure 6.** The cumulative distribution of  $\chi^2$  obtained from  $10^3$  random mock data sets drawn from the ergodic  $F_u$  for an NFW halo with  $M_{200} = 5 \times 10^8 M_\odot$  with a concentration  $C = 0.6\bar{C}$ . The trimming radius is 10 kpc. The vertical line indicate the value obtained from the observations for the same halo model.

**Table 1.** Upper limits on the mass of NGC1052-DF2. Masses are in units of  $10^9 M_\odot$ .

CL	(10, 0.6)		$(r_{\text{tr}}/\text{kpc}, C/\bar{C})$		(20, 0.6)	
	$M_{200}$	$M_{10\text{kpc}}$	$M_{200}$	$M_{10\text{kpc}}$	$M_{200}$	$M_{10\text{kpc}}$
$1\sigma$ (68%)	2.9	1.5	1.7	1.4	0.12	0.12
$1.64\sigma$ (90%)	8.1	2.7	4.3	3.3	1.8	1.1
$2\sigma$ (95%)	15.2	3.8	7.9	5.0	3.8	1.7

## 5 DISCUSSION AND CONCLUSIONS

We have employed the phase space distribution function to show that the kinematics of NGC1052-DF2 is compatible with a dynamical mass on the order of a few  $10^{10} M_\odot$ . The assumed NFW mass model we adopt is consistent with the structure of halos found in cosmological simulations of the  $\Lambda$ CDM model. The model relies on (possibly cumulative) action of tidal stripping events for the removal of matter beyond a distance 10 kpc from the center of NGC1052-DF2. Our findings here are consistent with a model in which NGC1052-DF2 started as a normal DM halo, but had its matter beyond  $\sim 10$  kpc removed by external gravitational tides. Alternatively, the progenitor of NGC1052-DF2 could have always been under the influence of an external gravitational field, preventing its growth beyond a certain radius. In both of these scenarios, the inner regions maintain most of their mass and do not undergo major disruption of their internal cold kinematics (Ogiya 2018; Wasserman et al. 2018).

In a previous paper (Nusser 2018), it was demonstrated that a low dynamical mass for NGC1052-DF2 leads to short orbital decay times by dynamical frictions. The high mass limits obtained

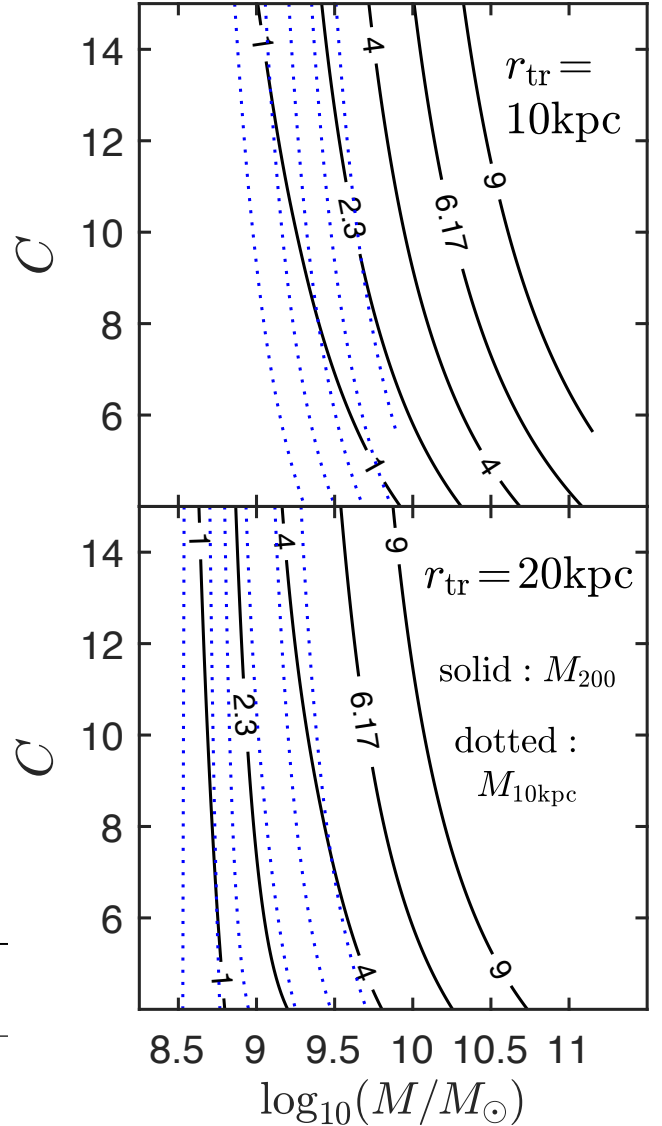


**Figure 7.** Contour maps of  $\Delta\chi^2$  in the plane of the concentration  $C$  and mass. Solid and dotted contours correspond, respectively, to  $M_{200}$  and  $M_{10\text{kpc}}$ . The top and bottom panels represent results for NFW profiles trimmed, respectively, at  $r_{\text{tr}} = 10$  kpc and 20 kpc. The results are obtained assuming an ergodic DF. Numeric values are indicated on the solid contours only. Dotted contours correspond to the same CLs.

here resolve this issue by increasing the dynamical friction time scales by a factor 5 or so. However, the question arises whether the analysis, based on the assumption of a steady state, remains valid at low masses in light of the importance of dynamical friction. The dynamical time scale for small masses is short compared to the Hubble time but it is still longer than the dynamical time of the system. Thus we expect the analysis to remain valid even at small masses. We mention in passing that the numerical tests of the previous paper, confirm that dynamical friction has very little effect on the velocity dispersion. Recently, Yu et al. (2018) identified “galaxies” in the Illustris simulations (Gené et al. 2014) having very little dark matter. This is an interesting finding, but it may not actually be



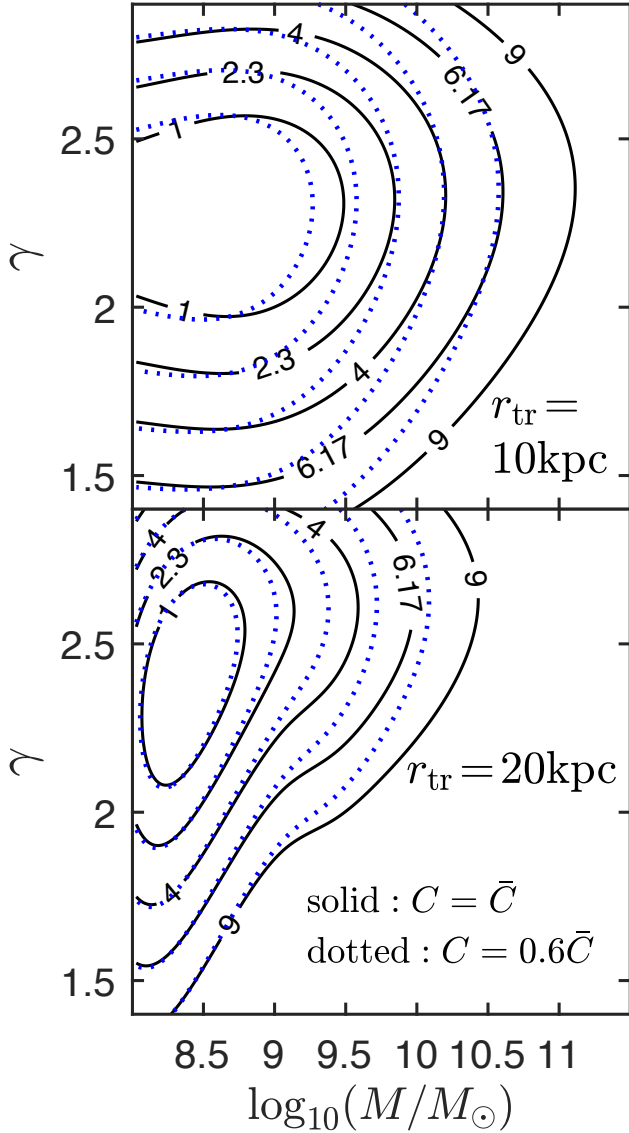


**Figure 8.** Contour maps of  $\Delta\chi^2$  as a function of  $\gamma$  and  $M = M_{200}$  obtained from the ergodic DF. Solid and dotted contours correspond, respectively, to  $C = 0.6C_{\text{mean}}$  and  $C = C_{\text{mean}}$ .

relevant to NGC1052-DF2 because of the short dynamical friction time scale obtained for low dynamical mass.

Both Wasserman et al. (2018) and Hayashi & Inoue (2018) performed a Jeans analysis based on the velocity dispersion predicted from a mass model. They both assumed a tracers' distribution consistent with a projected Sérsic profile. However, the conclusions of these two groups are different. Wasserman et al. (2018) provide dynamical mass-light-ratio  $1.7^{+0.7}_{-0.5} M_{\odot}/L_{\odot,V}$ , while Hayashi & Inoue (2018) argue that the NGC1052-DF2 mass remains uncertain due to the unknown distribution of tracers. Hayashi & Inoue (2018) also find that with Sérsic based tracers' distribution, a boost by a factor of 5 in the mass within 7.6 kpc is achieved in comparison to a power law with  $\gamma \sim 1$ . Here, we opted to work with a power law for form  $\nu \sim r^{-\gamma}$  and estimate  $\gamma$  using the likelihood function. Given the small number of star clusters used as mass tracers, we feel that this simple form is quite ade-

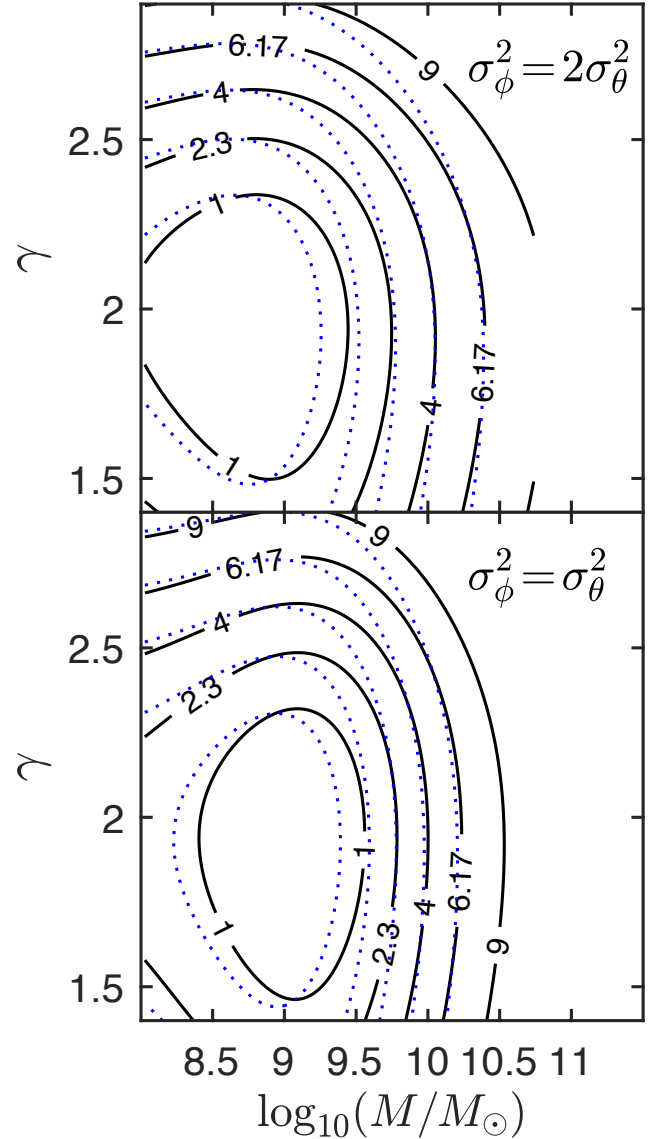


**Figure 9.** Contour of  $\Delta\chi^2$  for NFW mass profile obtained from DF with circular for isotropic (bottom) and non-isotropic (top) angular distribution of tracers. As in the previous figures,  $R_{\text{trim}} = 10$  kpc and the solid and dotted contours correspond to low and high concentrations.

quate. A much more important effect is related to the reduction of velocity dispersion by the removal of fast particles penetrating the inner regions from the outer regions.

The  $2\sigma$  upper limit of  $1.5 \times 10^{10} M_{\odot}$  on the mass of NGC1052-DF2 is a factor 4–5 below the SHMR (Behroozi et al. 2010; Moster et al. 2013; Rodríguez-Puebla et al. 2017), where at the relevant mass scale, the scatter in the relation is about 0.36 dex (Wasserman et al. 2018). We should also keep in mind that the inference of halo masses under the assumption of sphericity and steady state is associated with a factor of 2–3 uncertainties (e.g. Wang et al. 2017). Thus we conclude that the possibility that NGC1052-DF2 has a high mass consistent with the SHMR cannot be ruled out.

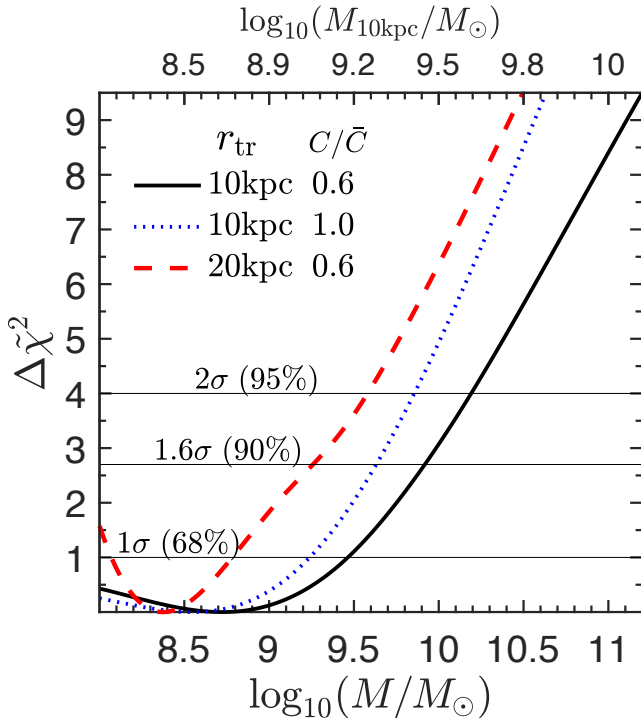


**Figure 10.** Curves of  $\Delta\chi^2$  as function of mass, for the ergodic DF. Solid and dotted lines are for  $r_{\text{tr}} = 10\text{ kpc}$  but with  $C/\bar{C}(M) = 0.6$  and 1, respectively. The red dashed curve is for  $r_{\text{tr}} = 20\text{ kpc}$  and the low  $C$  value. The bottom axis is the mass,  $M_{200}$  while the top axis is the mass within 10 kpc for  $C = 0.6\bar{C}(M)$ . For a given mass,  $\gamma$  is adjusted to its best-fit value,  $\gamma_M$ . Thin horizontal lines indicate CLs.

## ACKNOWLEDGEMENTS

This research was supported by the I-CORE Program of the Planning and Budgeting Committee, THE ISRAEL SCIENCE FOUNDATION (grants No. 1829/12 and No. 203/09) and the Asher Space Research Institute. The author acknowledges the hospitality of Department of Astronomy- Shanghai Jiao Tong University. The author is grateful to Asher Wasserman for providing him with the l.o.s velocities and projected distance of the 10 star clusters.

## REFERENCES

- Barnes J., Hut P., 1986, *Nature*, 324, 446  
 Behroozi P. S., Conroy C., Wechsler R. H., 2010, *ApJ*, 717, 379  
 Binney J., Tremaine S., 2008, *Galactic dynamics*. Princeton University Press, <http://adsabs.harvard.edu/abs/2008gady.book.....B>  
 Diemer B., Kravtsov A. V., 2015, *ApJ*, 799  
 Dutton A. A., Maccio A. V., 2014, *MNRAS*, 441, 3359  
 Gao L., Navarro J. F., Cole S., Frenk C. S., White S. D., Springel V., Jenkins A., Neto A. F., 2008, *MNRAS*, 387, 536  
 Gene S., et al., 2014, *MNRAS*, 445, 175  
 Hayashi K., Inoue S., 2018, *MNRAS*, 481L, L59  
 Ludlow A. D., et al., 2013, *MNRAS*, 432, 1103  
 Mamon G. A., Biviano A., Boué G., 2013, *MNRAS*, 429, 3079  
 Martin N. F., Collins M. L. M., Longeard N., Tollerud E., 2018, *ApJL*, 859, L5  
 Moster B. P., Naab T., White S. D. M., 2013, *MNRAS*, 428, 3121  
 Navarro J. F., Frenk C. S., White S. D. M., 1996, *ApJ*, 462, 563  
 Nusser A., 2018, *ApJL*, 863, L17  
 Ogiya G., 2018, *MNRAS*, 480, L106  
 Rodríguez-Puebla A., Primack J. R., Avila-Reese V., Faber S. M., 2017, *MNRAS*, 470, 651  
 Sparre M., Hansen S., 2012, *JCAP*, 2012  
 Trujillo I., et al., 2018, eprint arXiv:1806.10141  
 Wang W., Han J., Cole S., Frenk C., Sawala T., 2017, *MNRAS*, 470, 2351  
 Wasserman A., Romanowsky A. J., Brodie J., van Dokkum P., Conroy C., Abraham R., Cohen Y., Danieli S., 2018, *ApJL*, 863, L15  
 Yu H., Ratra B., Wang F.-Y., 2018, *ArXiv Astrophys. e-prints*, 1809.05938  
 van Dokkum P., Danieli S., Cohen Y., Conroy C., 2018c, eprint arXiv:1807.06025  
 van Dokkum P., et al., 2018a, *Nature*, 555, 629  
 van Dokkum P., et al., 2018b, *ApJL*, 856, L30